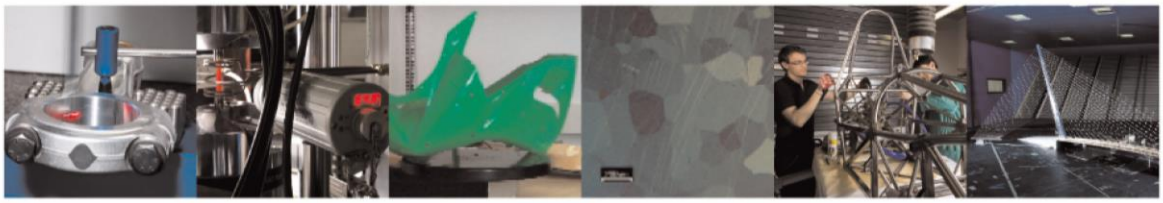

On the use of spatter signature for in-situ monitoring of Laser Powder Bed Fusion

REPOSSINI, GIULIA; LAGUZZA, VITTORIO; Grasso, Marco; Colosimo, Bianca Maria

This is a post-peer-review, pre-copyedit version of an article published in ADDITIVE MANUFACTURING. The final authenticated version is available online at: http://dx.doi.org/10.1016/j.addma.2017.05.004

On the use of spatter signature for in-situ Monitoring of Laser Powder Bed Fusion

Giulia Repossini, Vittorio Laguzza, Marco Grasso*, Bianca Maria Colosimo

Dipartimento di Meccanica, Politecnico di Milano, Via La Masa 1, 20156

**corresponding author, marcoluigi.grasso@polimi.it*

Abstract – In-situ monitoring of metal additive manufacturing (AM) processes is a key issue to determine the quality and stability of the process during the layer-wise production of the part. The quantities that can be measured via in-situ sensing can be referred to as "process signatures", and can represent the source of information to detect possible defects. Most of the literature on in-situ monitoring of Laser Powder Bed Fusion (LPBF) processes focuses on the melt-pool, laser track and layer image as source of information to detect the onset of possible defects. Up to our knowledge, this paper represents a first attempt to investigate the suitability of including spatter-related information to characterize the LPBF process quality. High-speed image acquisition, coupled with image segmentation and feature extraction, is used to estimate different statistical descriptors of the spattering behaviour along the laser scan path. A logistic regression model is developed to determine the ability of spatter-related descriptors to classify different energy density conditions corresponding to different quality states. The results show that by including spatters as process signature driver, a significant increase of the capability to detect under-melting and over-melting conditions is observed. This is why future research on spatter signature analysis and modelling is highly encouraged to improve the effectiveness of in-situ monitoring tools.

Keywords: Additive Manufacturing; Selective Laser Melting; in-situ monitoring; spatter; high-speed vision;

1. INTRODUCTION

Despite of rapid and continuous technological improvements, many metal Additive Manufacturing (AM) applications in relevant sectors, e.g. medical and aerospace, impose challenging quality and certification requirements that are still difficult to fulfil at the current maturity level. Indeed, different authors pointed out that limited process robustness, stability and repeatability represent a major barrier for the industrial breakthrough of metal AM systems [1 – 6]. Because of this, the development of in-situ sensing and process monitoring techniques has attracted the interest of researchers and AM system developers in the last few years (see Table 1). The challenge consists of quickly detecting the onset of defects by relying on in-situ gathered data, while the part is being produced. In [1], the measured quantities are referred to as "observable signatures", which enclose important information about the stability of the process and the quality of the additively produced part. This study focuses on Laser Powder Bed Fusion (LPBF) processes, also known as "Selective Laser Melting" (SLM). In LPBF, the observable signatures can be grouped into the following four major classes: i) the melt pool, ii) the track along the scan path, iii) the slice (i.e., the slice of the part scanned by the laser in each layer) and iv) the powder bed (i.e., the thin layer of loose powder

deposited by the recoating system). Table 1 summarizes the literature devoted to in-situ monitoring of LPBF processes based on these categories of process signatures[1].

Table 1 – Summary of the literature on in-situ LPBF process monitoring

Process signature	Literature in LPBF
Melt pool (size, shape, temperature)	[7] [8] [9] [10] [11] [12] [13] [14] [15] [16] [17] [18] [19]
Track along the scan path (geometry, temperature)	[20] [17] [21] [22] [23] [24] [25] [26]
Slice (surface pattern, geometry, thickness, temperature)	[27] [28] [29] [30] [31] [32] [33] [25] [22]
Powder bed (homogeneity)	[31] [32] [34] [35]

The melt pool is formed during the laser irradiation of the powder and then solidifies to the consolidated structure. Its stability, size and behaviour determine to a great extent the quality and stability of the process [36]. Additional information can be gathered at track level, including the geometry and the temperature profile of each track along the scan path, which are relevant to detect balling phenomena [37], lack-of-fusion and local over-heating. By expanding the region of interest, it is possible to characterize the entire slice in terms of surface patterns, geometry, thickness and temperature profiles. This allows determining not only the accuracy of the each slice compared with the CAD model, but also the existence of internal defects [31, 22]. Eventually, the powder bed homogeneity represents a further signature of the LPBF process that influences the laser beam-material interaction and the occurrence of local defects [31 – 32]. Although most of the studies mentioned in Table 1 focused on one category of signatures at a time, multi-sensor data fusion techniques could be used, in principle, to achieve a more complete process characterization by combining information coming from different sources. In this framework, co-axial sensing can be used to monitor the melt pool stability over time, whereas off-axial sensing can be used to monitor additional quantities that can not be measured by exploiting the optical path of the laser. This motivates the analysis of novel process signatures to enhance the comprehension of LPBF phenomena and the quick detection of defects. In particular, this study investigates the suitability of material ejections produced by the beam-material interaction as observable signatures. Previous studies [23 – 24] showed that track-related information that can be acquired via in-situ sensing include the amount of ejected material and the overall spattering behaviour. The spatter generation mechanism was studied by Liu *et al*. (2015) [38] and Khairallah *et al*. (2016) [39], who pointed out the existence of two kinds of spattering phenomena. One is caused by a convective transport of liquid or vapourized metal out of the melt pool, known as “droplet spatter”. Another one, known as “powder spatter” is caused by non-melted metallic powder particles blown away as a result of the impact of the metallic vapour. The physical description of the spatter generation mechanism goes beyond the purpose of our study, and we refer the interested reader to [38] and [39] for additional details. Our aim consists of investigating whether spatter-related information can be used as a further driver for process

[1] For a more detailed classification and discussion of the literature see [45].

stability analysis and to detect unwanted process conditions, in addition to other measurable quantities investigated in the literature. Some authors [40] showed that spatters may produce inclusions and discontinuities in the material, together with irregularities of the powder bed. However, there is a lack of studies on the measurement and the use of spatter-related information for monitoring purposes in laser-based additive manufacturing. A more consolidated literature on this topic can be found in laser welding applications, where various authors [41 – 44] showed that different descriptors of the spattering behaviour can be used to determine the process quality and stability. Despite various differences between LPBF and laser welding, those studies provide relevant guidelines for the characterization and the quantification of the spattering behaviour via in-situ signal analysis.

Following the seminal contribution of Bayle and Doubenskaia (2008) [24] and Lane *et al*. (2014) [23], this study aims to evaluate the suitability of spatter-related information acquired in-situ via high-speed machine vision for the development of in-process monitoring tools. Analogously to the studies of Gao *et al*. (2013) [41] and You *et al*. (2014) [44] in laser welding, a methodology for image segmentation and statistical descriptor estimation (including spatter area, number, spatial spread, etc.) is proposed. Gao *et al*. (2013) [41] used these descriptors to classify portions of the weld seam having out-of-control bead width. In this study, instead, the analysis is extended to LPBF, in order to determine the effect of process parameters on the spattering behaviour and to classify different energy density levels that yield out-of-control quality characteristics. Moreover, a new method to determine the spatial spread of the spatters while the laser beam moves along the scan path is proposed, and the relevance of spatter-related descriptors is investigated by means of a logistic regression classification model [46]. A comparative analysis shows that the in-situ characterization of process spatters enhances the classification between different melting conditions (under-, normal and over-melting) with respect to the analysis of the laser heated zone alone. This makes the spatter behaviour one additional suitable signature of the LPBF process, to be possibly combined with other well-known quantities, e.g. the melt pool size, shape and temperature, to enhance process monitoring tools.

The remaining of the paper is organized as follows. Section 2 presents a real case study and the in-situ monitoring setup; Section 3 describes the image processing methodology; Section 4 presents the achieved results and Section 5 concludes the paper.

2. REAL CASE STUDY

In order to acquire and characterize the spatter-related information during an LPBF process, an experimental study was carried out, involving the production of specimens with different sets of process parameters. Sub-section 2.1 introduces the experimental plan, sub-section 2.2 describes the in-situ sensing setup for high-speed image acquisition and sub-section 2.3 provides a brief characterization of the as-built part properties.

2.1. Experimental plan

The case study involves the production of two builds by varying the process parameters. In each build, nine specimens where produced via LPBF of 18Ni (300) maraging steel powder (see Appendix B for material specifications) corresponding to three energy density levels, with three replicates for each level. The energy density, i.e., the energy per surface (or volume) unit transferred to the material during the laser scanning of each layer, is a synthetic parameter whose correlation to the part quality was investigated by several authors [1, 37, 40]. In this study, such synthetic parameter was used to induce both quality and defective parts and to test the spattering behaviour under different melting conditions.

The two builds differ in terms of layer thickness (respectively $z = 40\ \mu m$ and $z = 50\ \mu m$) and spatial allocation of different energy density levels on the baseplate (see Fig. 1).

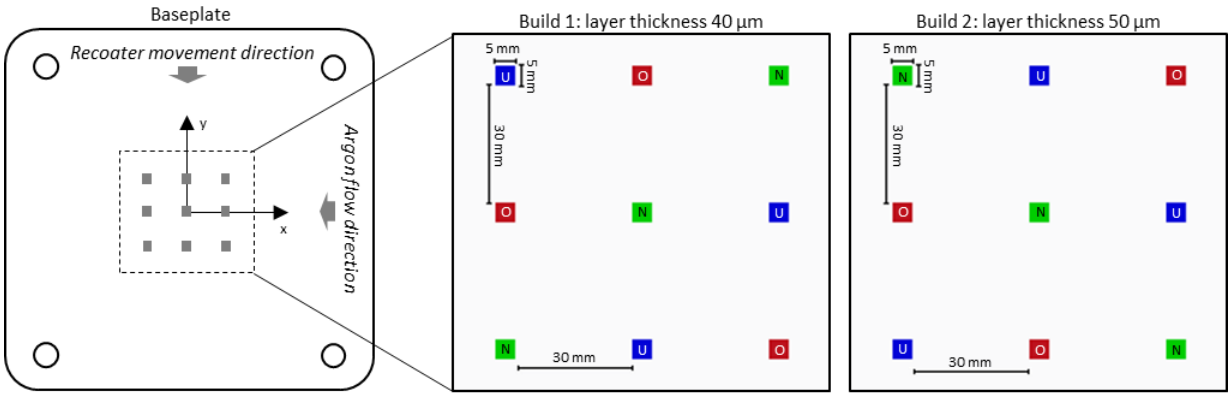

Fig. 1 – Scheme of specimen allocation on the baseplate; U (blue): under-melting, N (green): normal-melting, O (red): over-melting

Each specimen is a parallelepiped of size $5 \times 5 \times 12\ mm$ produced by applying a stripe scanning strategy, with a 67° scan direction rotation every layer. The specimens were placed in the middle of the platforms (Fig. 1), at a sufficient distance from each other to guarantee no thermal interference. The randomized spatial location of the specimens were selected accordingly to two 3×3 Latin square designs, one for each build, where each energy density level occurs once in each row and column.

The energy density levels were controlled by the volumetric fluency, F, defined as follows:

$$F = \frac{tP}{d_h d_p z} \qquad \left[\frac{J}{cm^3}\right] \tag{1}$$

where: t $[\mu s]$ is the laser exposure time, P $[W]$ is the laser power, d_h $[\mu m]$ is the hatch distance, i.e., the distance between adjacent hatches, d_p $[\mu m]$ is the distance between adjacent points along each hatch, and z $[\mu m]$ is the layer thickness. The laser spot diameter at the powder layer is 70 μm.

The intermediate energy density level, hereafter referred to as “normal melting”, corresponds to the default set of parameters suggested by the LPBF system (Renishaw AM250) developer. The lower (called “under-melting”) and upper (called “over-melting”) energy density levels were set by varying the laser exposure time, with values that depend on the layer thickness. Table 2 summarizes the controlled parameters and the resulting volumetric fluency. All other process parameters were set at default values and kept fixed for all the produced specimens.

The parameters shown in Table 2 refer to the scan of internal hatches. The scan of borders and top surfaces, instead, exploits default parameters that are equal for all the specimens ($P = 100\ W$, t = 50 μs, $d_p = 20\ \mu m$).

Table 2 – Process parameters used in different energy density levels

Build	Energy density level	t $[\mu s]$	d_p $[\mu m]$	d_h $[\mu m]$	P $[W]$	z $[\mu m]$	F $[J/cm^3]$
1	Under-melted	42	65	80	200	40	$4*10^4$
	Normal-melted	83	65	80	200	40	$8*10^4$
	Over-melted	125	65	80	200	40	$12*10^4$
2	Under-melted	52	65	80	200	50	$4*10^4$
	Normal-melted	104	65	80	200	50	$8*10^4$
	Over-melted	156	65	80	200	50	$12*10^4$

2.2. In-situ sensing setup

The in-situ image acquisition equipment consists of a high-speed camera (Olympus I-speed 3 with CMOS sensor) in the visible range (about 400 to 700 nm) placed outside the protective window[2] of the building chamber as shown in Fig. 2.

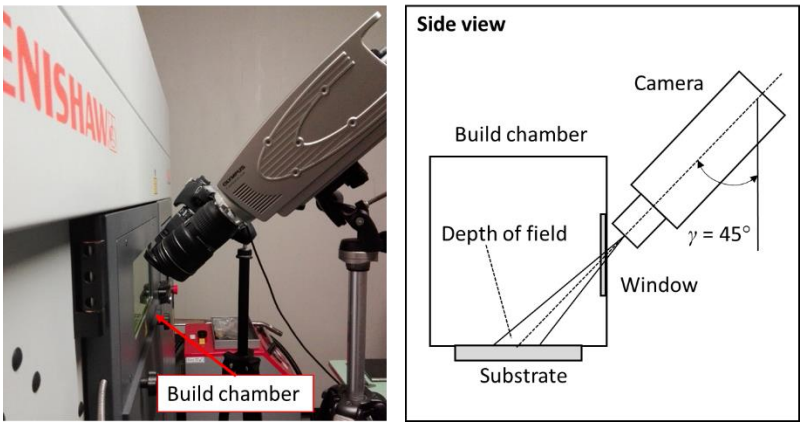

Fig. 2 – Off-axial mounting of the high-speed camera outside the build chamber

[2] The protective windows filters out the laser wavelength of 1070 nm.

Such a monitoring setup is called “off-axial” in the AM literature [21], because the data acquisition is performed outside the optical path of the laser, and it is suitable to capture images over a field-of-view that is larger than the scanned area. The high-speed camera was equipped with a Tamron SP 17-50 mm F/2.8 lens, and the images were acquired at 1000 frames per second, in order to capture the spattering behaviour with a sufficient temporal resolution. A higher acquisition speed could improve the characterization of very fast laser-material interaction dynamics, but this comes at the expense of spatial resolution and real-time computational feasibility. Therefore, the frame rate should be chosen as a compromise between the reduction of information loss on the one hand, and the feasibility of analyzing the image stream during the process with reasonable computational resources and sufficient spatial resolution. After preliminary experimentations, an acquisition speed of 1000 frames per second turned out to be a reasonable choice. A chessboard camera calibration was performed to estimate the spatial resolution in the powder bed plane, which was about 250 µm/pixel. However, the calibration is not suitable to determine the actual size of spatters that move in any direction above that plane. Because of this, only the apparent spatter size can be measured and expressed in pixel units. The spatter trajectory mainly depends on the inert gas (argon) flow direction that is parallel to the window of the build chamber, from left to right, and on the laser scan direction that changes every layer. A study of the effect of the scan direction with respect to the camera on the apparent size of the spatters is discussed in Section 3.

The total number of layers was 300 in Build 1 ($z = 40\ \mu m$) and 240 in Build 2 ($z = 50\ \mu m$). The data discussed in this study refer to a subset of them, with a step of about 30 layers between two consecutively monitored layers. The image acquisition started after the 20th layer in order to avoid the inclusion of transitory phenomena during the very first few layers, where the process is not yet in regime conditions. In addition, because of a field of view limitation imposed by the monitoring setup, the analysis of image-based descriptors presented in the study refer to the upper row of both the builds. This also allows comparing descriptors from different energy density levels being equal the distance of the slice from the camera. Future studies should investigate in more depth the spatial location effect on in-situ spatter analysis.

2.3. As-built part characterization

The specimens produced with different energy density levels exhibit different quality properties. Fig. 3 shows the surface patterns of top layers for all the specimens in the two builds. Fig.3 provides a first evidence about the effect of the energy density on the regularity of the melting along the tracks. The most severe irregularity was observed in the presence of over-melting conditions, especially in Build 2 ($z = 50\ \mu m$). The under-melting state produced some irregularity of smaller severity, with different surface pores of diameter up to $150\ \mu m$, although few surface pores were observed also under normal melting conditions.

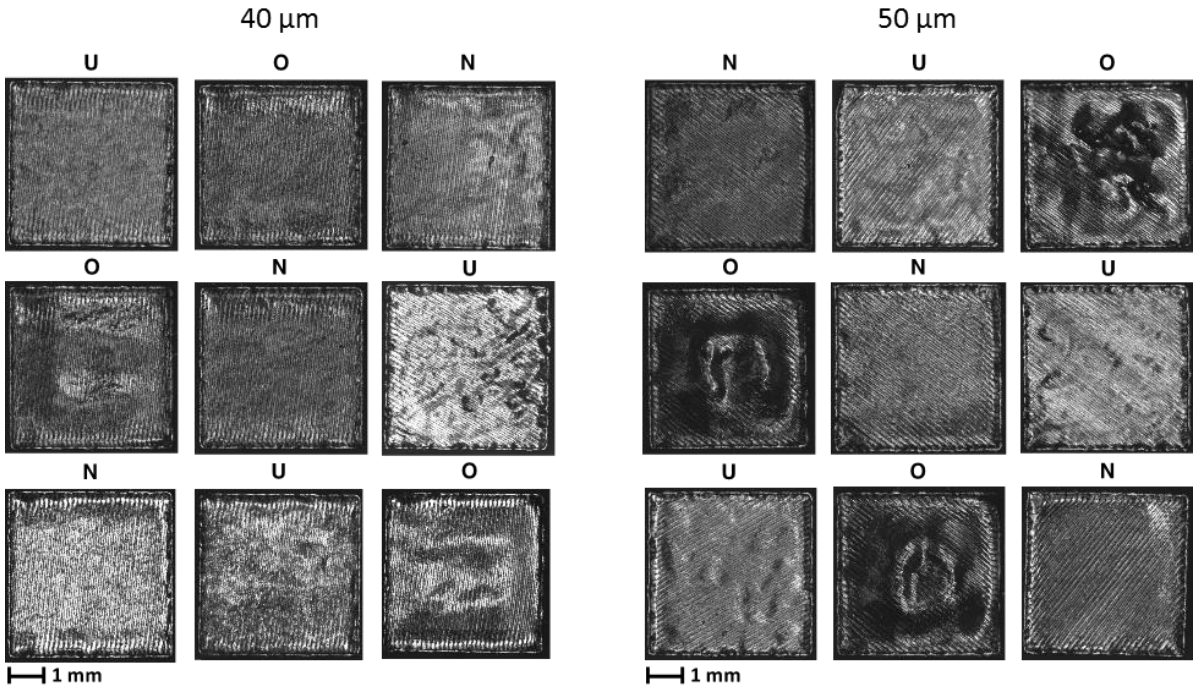

Fig. 3 – Surface patterns (top layer) of LPBF-produced specimens; U: under-melted, N: normal-melted, O: over-melted

In order to evaluate the final part density, the Archimede's test was performed and the main results are shown in Fig. 4. Fig. 4 shows the main effect plot of three factors on the part density: i) the energy density, ii) the specimen location along the X axis and the iii) specimen location on the Y axis. The only statistically significant factor is the energy density in both the builds, with goodness-of-fit $R^2_{adj} = 99.57\%$ in Build 1 and $R^2_{adj} = 89.63\%$ in Build 2. In normal-melting conditions, the largest average density was obtained (larger than 98.5%), whereas the under-melting condition yielded the lowest density (slightly more than 93% in Build 1). The Tuckey's multiple comparison test [47] between the energy density levels showed that, in Build 1 ($z = 40\ \mu m$), normal and over-melting levels are not statistically different, which complies with the similar surface patterns in Fig. 3 (left panel). On the contrary, in Build 2 ($z = 50\ \mu m$), the normal-melting conditions produces a part density that is statistically different from both the other two melting states. This is probably due to the fact that, although the volumetric fluency is equal in the two builds, the different exposure times combined with a different layer thickness influence in a dissimilar way the relative quality characteristics. Eventually, the non-significant effect of the spatial location along the X and Y axes on the part quality allows one to neglect any location effect in the following analysis.

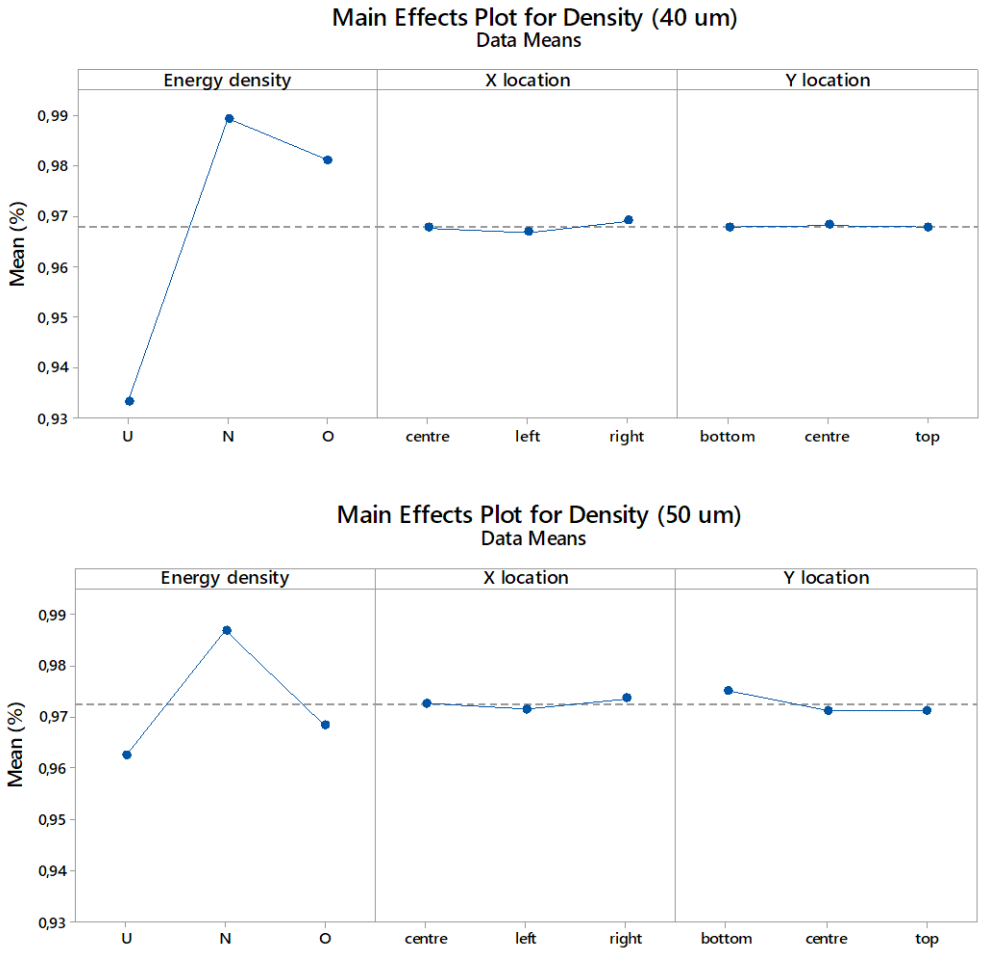

Fig. 4 – Main effect plots for the part density in Build 1 (top panel) and Build 2 (bottom panel); U: under-melted, N: normal-melted, O: over-melted

3. IMAGE SEGMENTATION METHODOLOGY

Each acquired frame consists of a dark background and different hot (white) spots in foreground. Those hot spots correspond to the light emitted by the spatters and the laser heated zone (LHZ). The LHZ is the area of the slice that encloses and extends beyond the melt pool, which emits light captured by the camera sensor in the visible range. The aim of the proposed image processing methodology consists of describing each hot spot as a distinct connected component of the image and estimating its relevant descriptors. This methodology includes the following sequential steps. First, the original grey-scale images are converted into a binary format by means of a thresholding algorithm and the connected components are identified and isolated (step 1). The next step consists of classifying every connected component either as a spatter or the LHZ (step 2). Eventually, different statistical descriptors are estimated for the spatters and LHZs in all the monitored frames (step 3). It is worth noticing that no classification between droplet and powder spatters is envisaged. Indeed, the aim of the study consists of capturing the signature of the spattering behaviour as a whole, and to evaluate how different process conditions affect such a signature. A brief description of each step is discussed in the following.

Step 1 – Thresholding

Image thresholding is needed to separate the foreground components from the background. In [48] several existing thresholding methods were divided into the following categories: histogram-based, clustering-based, entropy-based, attribute-based, spatial and local approaches. A comparison of most of them in different benchmark applications was discussed in [48] and [49], where the authors pointed out that the thresholding performances usually depend on the nature and properties of the original image. In this study, the images exhibit a bimodal histogram, with foreground and background intensities well separated apart. In such condition, most thresholding methods are known to provide good results. In particular, the Otsu's method [49] was chosen in this study, being the most common choice in the presence of bimodal image histograms. The output of the thresholding operation is a binary image, where every foreground area is isolated and treated as a distinct connected component.

Step 2 – Classification

After the segmentation, the classification between spatters and LHZs is performed for each acquired image. To this aim, a method based on two criteria is proposed. The first classification criterion regards the area of the connected components. The analysis of video frames and the literature in laser welding [41 – 44] highlights that the LHZ is typically larger than the spatters. Because of this, analogously to the image processing techniques discussed by other authors [41, 44], it is possible to set a threshold on the area of the connected components for classification purposes. However, a more reliable approach consists of coupling an area-based criterion with a position-based one. Indeed, the LHZ is expected to be not only the larger connected component in the image, but its centroid must be located in the proximity of the area of the layer that is currently scanned by the laser. Therefore, it is possible to determine a region of interest that should enclose the LHZ, and classifying as LHZ the largest connected component that is partially or fully included within that region. In this study, the region of interest correspond to the nominal slice area of the specimens in each layer. More accurate results can be achieved in future analysis if the actual position of the laser can be made available and synchronized with the image acquisition.

Fig. 5 shows a superimposition of all the centroids of connected components classified as either spatters (red) or LHZs (black) extracted from the images streams associated to the normal melting condition in Build 1.

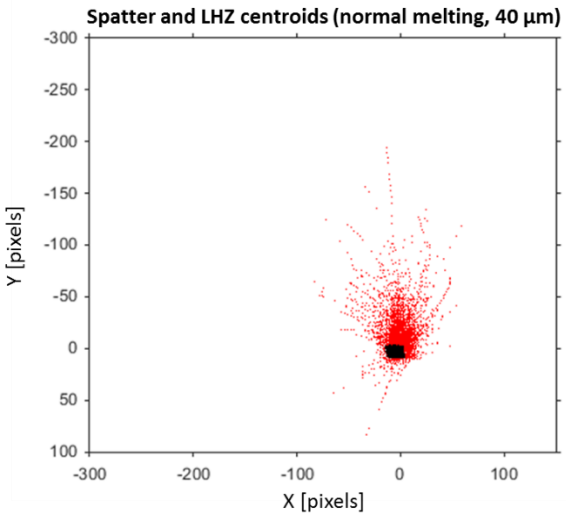

Fig. 5 – Superimposition of the centroid of every connected component classified as spatter (red) or laser heated zone (black), under normal melting condition (Build 1)

Notice that the spatter visibility is related to its temperature. When the spatters are hot, the emitted light is captured by the camera, but as they fly away from the melt pool along their trajectory they cool down until the emitted light becomes too low to be captured by the camera sensor. Because of this, the observed spatial spread of the spatters can be related both to the time the particle temperature remains above a visibility threshold and to the ejection velocity.

Fig. 6 shows the coordinates of LHZ centroids during the LPBF of one layer of a normal melted specimen (Build 1) along the X and Y directions. Different colours are used to indicate the internal hatches (blue) and the border hatches (red) covered along the overall scan path. Fig. 6 shows that the classification between LHZ and spatters allows reconstructing the actual trajectory of the laser beam. The noisy pattern of the reconstructed trajectory is mainly due to the varying shape of the LHZ from one frame to the following one, which influences the determination of the LHZ centroid. The capability of reconstructing the actual LHZ trajectory is a qualitative mean to assess the goodness of the classification algorithm.

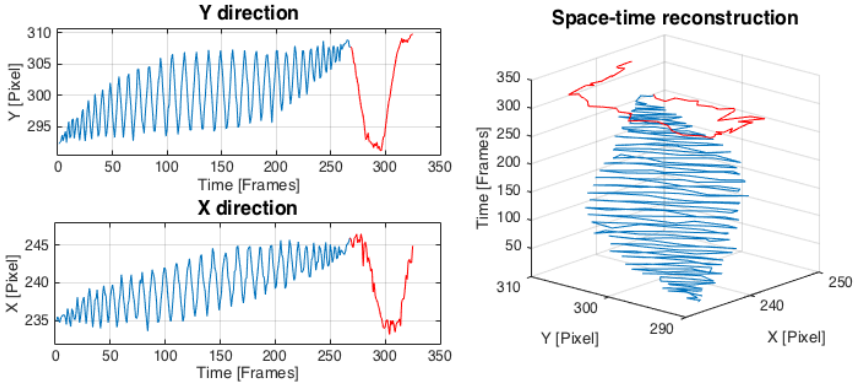

Fig. 6 – Example of LHZ centroid coordinates during the LPBF of one layer (normal-melted specimen); the coordinates along internal hatches are shown in blue and the coordinates along the slice contour are shown in red

Step 3 – Statistical descriptors

Let $\boldsymbol{\mathcal{U}} = \{\boldsymbol{U}_1, \boldsymbol{U}_2, \dots, \boldsymbol{U}_J\} \in \mathbb{R}^{J \times M \times N}$ be the three-dimensional array that represents the image stream acquired during the LPBF of one slice, where J is the total number of acquired frames, and $M \times N$ is the size, in pixels, of each frame. The j-th frame, $\boldsymbol{U}_j \in \mathbb{R}^{M \times N}$, $j = 1, \dots, J$, is such that the (m, n)-th element of the matrix represents the intensity of that pixel in the corresponding frame, for $m = 1, \dots, M$ and $n = 1, \dots, N$. After image segmentation and connected component classification, each frame includes N_j foreground components classified as spatters and one component classified as LHZ.

The following statistical descriptors were computed for the spatters: i) the number of spatters in the j-th frame, N_j, ii) the average area of all the spatters in the j-th frame, $\bar{A}_j = (1/N_j) \sum_i A_{i,j}$, where $A_{i,j}$ is the area if the i-th spatter in the j-th frame, and iv) the area of the convex hull that encloses all the spatters in the j-th frame, $A_{CH,j}$. They describe the spattering behaviour in terms of number, size and spatial spread, respectively. The convex hull is defined as the smallest convex polygon that contains all the connected components classified as spatters. The farther are the spatters from the LHZ, the larger is the area of the corresponding convex hull, which is then used as a proxy of the spatter spatial spread.

In addition to the spatter descriptors, the LHZ is described in terms of its area, $A_{LHZ,j}$, for $j = 1, \dots, J$. Monitoring the LHZ area along the scan path of the laser is representative of monitoring approaches proposed in the literature by using either co-axial or off-axial sensing setups [1], and hence this additional descriptor represents a benchmark for the following analysis.

4. DISCUSSION OF RESULTS

This section presents the main results achieved by applying the proposed image analysis methodology to the case study described in Section 2. Sub-section 4.1 first describes how different energy density levels and other factors influence the marginal and joint distribution of the selected descriptors. Then, sub-section 4.2 demonstrates the benefits achieved by using the spatter-related information to classify different melting conditions.

4.1. Spatter behaviour characterization

Fig. 7 and Fig. 8 show the scatterplots of the four statistical descriptors for Build 1 and Build 2, respectively, where different colours indicate different melting conditions, i.e., under-, normal and over-melting. The main diagonal of Fig. 7 and 8 shows the histograms of each descriptor and other panels show the pairwise scatterplots. The data from all the acquired videos are shown, with no distinction between data points corresponding to internal or border hatches. The histograms show that normal, over- and under-melting conditions produce not only a modification of the means of single descriptors, but also a modification of their variance and overall probability distribution (e.g., see the number of spatters and the convex hull area in Fig.

8). The scatterplots represent the correlation between different descriptors. They show that, despite a partial overlap, different conditions yield a different spread of the descriptors in the bivariate sub-spaces. This allows identifying different patterns of the spattering behaviour to classify the current melting state.

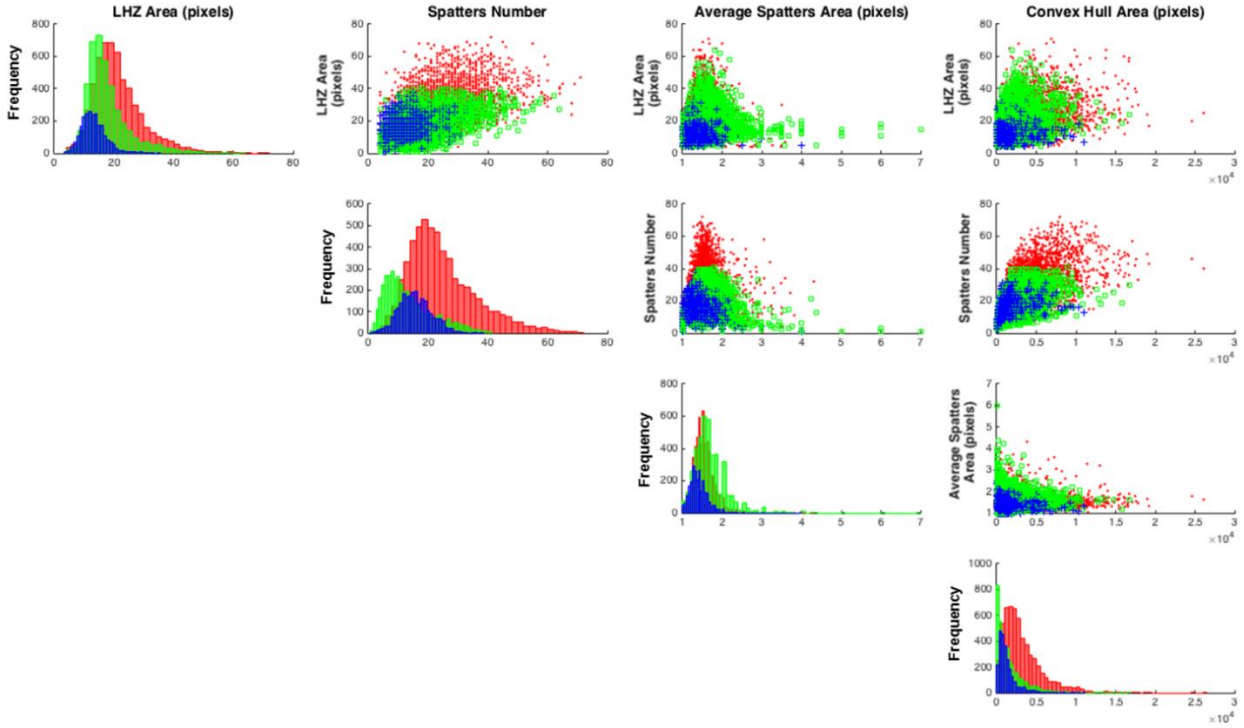

Fig. 7 – Scatterplot of spatter and LHZ descriptors (Build 1); blue crosses: under-melted, green squares: normal-melted, red circles: over-melted

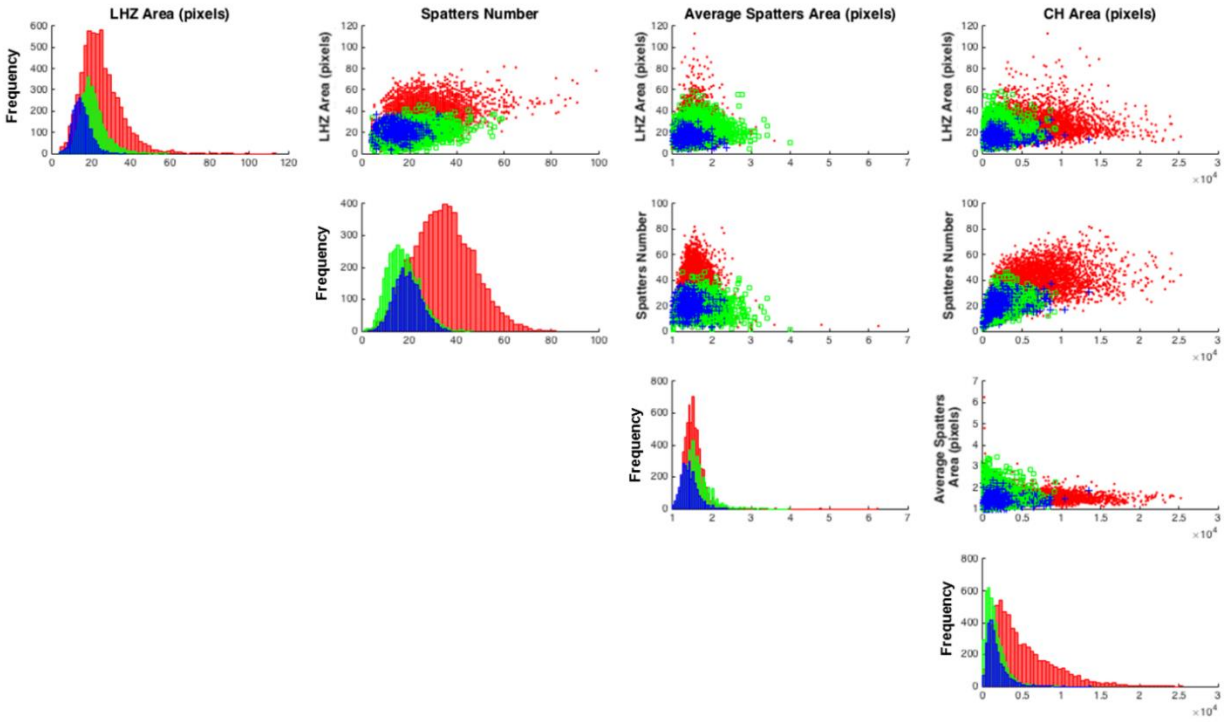

Fig. 8 – Scatterplot of spatter and LHZ descriptors (Build 2); blue crosses: under-melted, green squares: normal-melted, red circles: over-melted

Generally speaking, the over-melting state yields the largest dispersion of all the descriptors with the only exceptions of the average spatter area, $\bar{A}_j$. Fig. 9 shows a comparison of the pattern of spatter spatial spread under different melting conditions in the two builds included in our experimentation. Fig. 9 shows the larger spread achieved in the presence of the over-melting state.

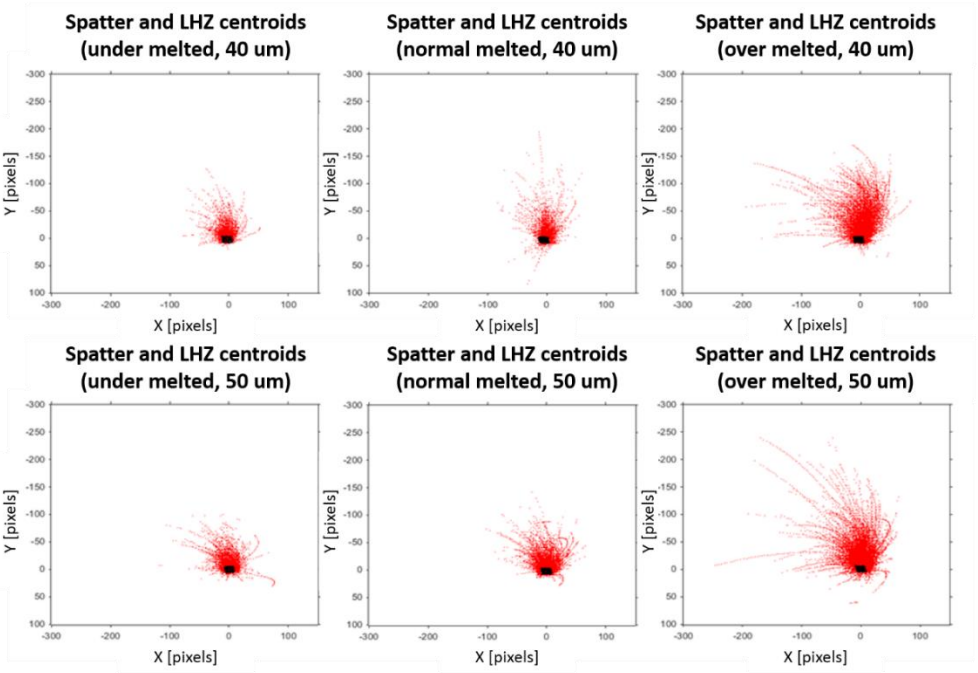

Fig. 9 – Superimposition of the centroid of every connected component classified as spatter (red) or laser heated zone (black), under different melting conditions (top panels: Build 1, bottom panels: Build 2)

Table 3 – p-values of the Pearson's correlation test between pairs of statistical descriptors

Build 1 ($z = 40\ \mu m$)						
	N		$\bar{A}$		A_{CH}	
A_{LHZ}	Under-melted	0.000	Under-melted	0.005	Under-melted	0.022
	Normal melted	0.000	Normal melted	0.824	Normal melted	0.000
	Over-melted	0.000	Over-melted	0.000	Over-melted	0.000
N			Under-melted	0.000	Under-melted	0.000
			Normal melted	0.000	Normal melted	0.000
			Over-melted	0.000	Over-melted	0.000
$\bar{A}$					Under-melted	0.000
					Normal melted	0.000
					Over-melted	0.000
Build 2 ($z = 50\ \mu m$)						
	N		$\bar{A}$		A_{CH}	
A_{LHZ}	Under-melted	0.000	Under-melted	0.4110	Under-melted	0.001
	Normal melted	0.000	Normal melted	0.173	Normal melted	0.000
	Over-melted	0.000	Over-melted	0.000	Over-melted	0.000
N			Under-melted	0.594	Under-melted	0.000
			Normal melted	0.001	Normal melted	0.000
			Over-melted	0.000	Over-melted	0.000
$\bar{A}$					Under-melted	0.000
					Normal melted	0.066
					Over-melted	0.001

The correlation between each pair of descriptors is quantified in Table 3, which summarizes the Pearson' correlation test p-values for each energy density condition. Table 3 shows that the most significant correlation exists between the following pairs of descriptors: (A_{LHZ}, N), (A_{LHZ}, A_{CH}) and (A_{CH}, N). Indeed, an increase of the energy density yields an increase of both the sample mean and variance of the number of spatters, their spatial spread (convex hull area) and the area of the LHZ. The average spatter area, $\bar{A}$, exhibits a different behaviour, although it is significantly correlated to N and A_{CH} in Build 1.

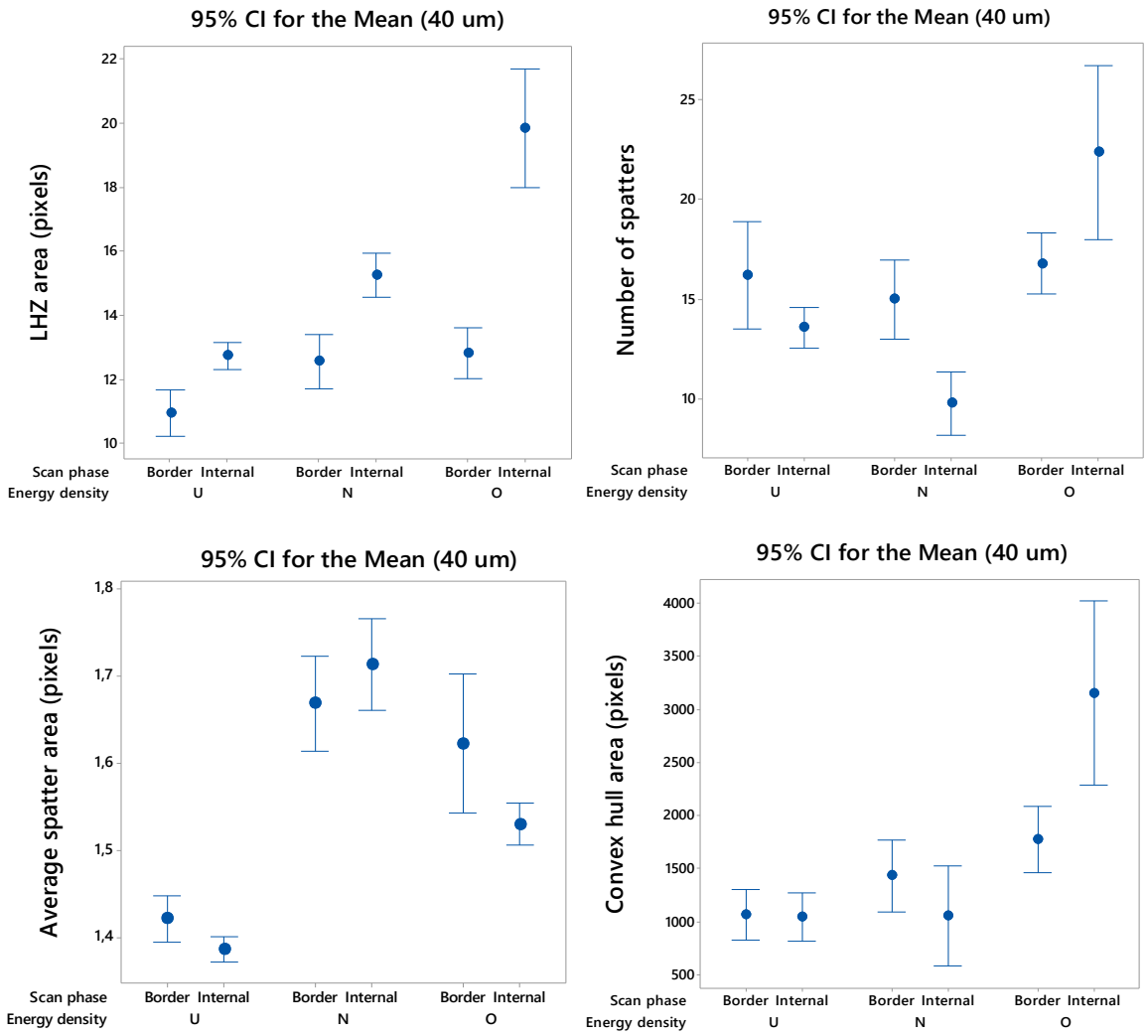

Fig. 10 – 95% CIs of mean spatter and LHZ descriptor values as a function of the scan phase and the energy density (Build 1)

The effect of both the scan phase and the energy density on each single descriptor is better highlighted in Fig. 10, where the 95% confidence intervals (CIs) for the mean descriptors are shown[3], and in Table 4, where

[3] Due to the significant correlation between the sample mean and sample standard deviation of the descriptors, the major conclusions draw for the mean apply to the standard deviation as well.

the analysis of variance (ANOVA) results are summarized[4]. For sake of space, Fig. 10 shows the interval plots only for Build 1, as the major conclusions apply to Build 2 as well. The ANOVA was performed by including into the model also the scan angle, ϑ, i.e., the angle between Y axis and the scan direction, which changes every layer. Indeed, one purpose of the analysis was to determine whether the scan direction may influence the measurement of spatter descriptors. A reduced model is shown in Table. 4, which includes only the interaction between the energy density and the scan phase; other interactions were not significant and not included in the table for sake of clarity.

Table 4 : p-values of F-tests and goodness-of-fit for different spatters and LHZ descriptors; bold fonts are used to indicate statistically significant terms at family-wise $\alpha = 0.05$

Build	Source	Responses			
		A_{LHZ}	N	$\bar{A}$	A_{CH}
		R^2_{adj}=88.49%	R^2_{adj}=70.93%	R^2_{adj}=88.78%	R^2_{adj}=67.30%
Build 1 ($z = 40\ \mu m$)	Energy density	**0,000**	**0,000**	**0,000**	**0,000**
	Scan phase	**0,000**	0,025	**0,011**	0,614
	Scan angle (ϑ)	0,022	0,135	0,582	0,028
	Energy density*scan phase	**0,000**	**0,000**	**0,008**	**0,000**
		R^2_{adj}=91.59%	R^2_{adj}=80.87%	R^2_{adj}=57.04%	R^2_{adj}=71.64%
Build 2 ($z = 50\ \mu m$)	Energy density	**0,000**	**0,000**	**0,000**	**0,000**
	Scan phase	**0,000**	**0,000**	0,122	**0,000**
	Scan angle (ϑ)	0,022	0,167	0,505	0,060
	Energy density*scan phase	**0,000**	**0,000**	**0,001**	**0,000**

The energy density and its interaction with the scan phase significantly affect all the descriptors in both the builds. Generally speaking, the interaction between these two factors originates from the fact that the scanning of the border partially overlaps with the previously scanned internal hatches. Therefore, the laser-material interaction along the border in influences by the material properties caused by the energy density level adopted for the bulk part. However, the effect of the scan phase on the spatter descriptors depends on the layer thickness. Indeed, even if the volumetric fluency is kept fixed, a different exposure time coupled with a different layer thickness determines the spattering behaviour.

With regard to the scan angle, ϑ, no significant effect was observed on any of the analysed descriptors. This is explained by the fact that the spatter trajectory is mainly determined by the inert gas flow, that is perpendicular to the camera lens axis. This lack of significance allows studying the spattering behaviour in terms of the proposed descriptors regardless of the layer-wise changing scan direction.

The LHZ area, A_{LHZ}, enlarges as the energy density increases. As a matter of fact, the LHZ area is a proxy of the thermal energy transmitted by the laser to the material, as discussed by other authors [1]. The number

[4] This analysis separately applies to single responses; the overall significance of the factors was confirmed by means of a multivariate ANOVA analysis.

of spatters, N, observed in normal melting conditions is lower than the number in under- and over-melting. The spatial spread of the spatters measured by A_{CH} is not statistically different in under- and normal melting conditions, but it is significantly higher in the over-melting state. Eventually, the average spatter area, $\bar{A}$, exhibits a different behaviour from other spatter descriptors. Its highest value corresponds to the normal-melting condition. Both the under- and over-melting states yields statistically lower average areas, at least during the internal hatching phase, with the lowest average areas observed in under-melting conditions.

The main results of this exploratory analysis can be summarized as follows:

- The under-melting state yields a similar number of spatters to the one in normal-melting state, with a comparable spatial spread but with a smaller average area;
- The over-melting state yields a larger number of spatters than the normal-melting state with a larger spatial spread, but with a smaller average area;
- The LHZ area enlarges as the energy density increases.

These results suggest that monitoring the spattering behaviour via in-situ sensing may provide relevant information to determine the quality and stability of the LPBF process.

4.2. Classification of energy density levels

The previous analysis was aimed at exploring the effect of different factors and their interactions on the selected descriptors. The analysis presented in this sub-section, instead, aims at evaluating and demonstrating the suitability of spatter-related information to classify under- and over-melting conditions corresponding to low quality parts. Because of this, an ordinal logistic regression model was estimated [46]. The idea behind logistic regression consists of predicting the probability of different outcomes of a categorically distributed response variable, given a set of explanatory variables. In this study, the energy density is the categorical response with three levels that can be order in increasing fluency order. The explanatory variables are the spatter and LHZ descriptors, or a subset of them. The goal is not to determine which is the best classifier for our data, but to determine if the inclusion of spatter-related descriptors as predictor variables may enhance the classification of different energy density states. Because of this, the ordinal logistic regression model represents a suitable choice as it allows taking into account the ordinal nature of the dependent variable, evaluating the significance of different model terms and comparing alternative models by estimating goodness-of-fit measures. The details of the classification model are described in Appendix A.

Three ordinal logistic regression models were compared, by selecting different subsets of descriptors. The first model, representative of benchmark monitoring approaches, exploits the LHZ area alone as explanatory variable. The second model includes both the LHZ area and the spatter descriptors. The third model includes only the spatter descriptors. The classification models where compared in terms of both goodness-of-fit

criteria and misclassification performances. Regarding the goodness-of-fit estimation, two widely used criteria were applied: the Akaike Information Criterion (AIC) and the Bayesian Information Criterion (BIC) [50]. The AIC is defined as follows:

$$AIC = 2k - 2\ln(L) \tag{2}$$

where k is the number of parameters included into the model and L is the maximized value of likelihood function for the fitted model. The BIC applies a stronger penalization on the number of parameters with respect to the AIC and it is defined as follows:

$$BIC = -2\ln(L) + k\ln(n) \tag{3}$$

where n is the number of observations used to fit the model.

Fig. 11 shows the AIC and BIC values computed separately for the two builds, by including the measured values in all the monitored layers. Both for the criteria, the lower is the value of the test statistic, the more preferable is the model.

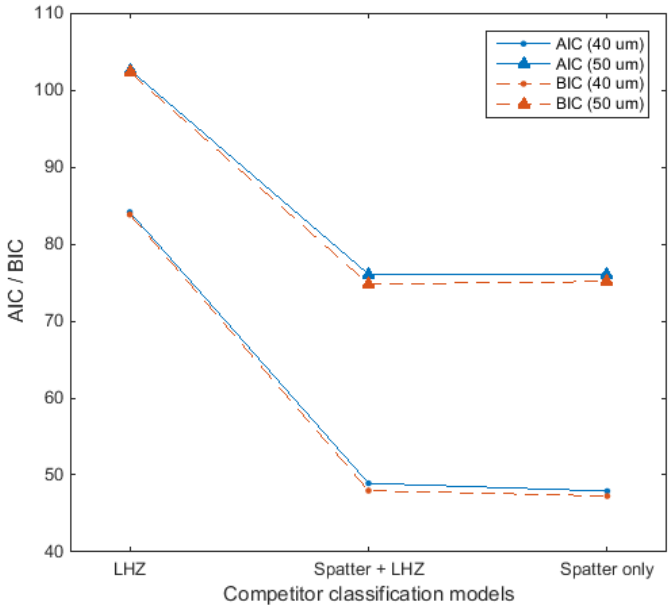

Fig. 11 – AIC and BIC values corresponding to different classification models

Fig. 11 shows that a classification model based on the LHZ area alone yields a lower goodness-of-fit than model that include the spatter descriptors as well. In addition, the two models that include only the spatter descriptors or the both the spatter and LHZ descriptors have a similar goodness-of-fit.

A further comparison was made by estimating the misclassification errors via leave-one-out cross-validation. The misclassification error is the overall ratio of wrongly classified energy density categories, ranging between 0 and 1. Fig. 12 shows the 95% CIs of misclassification errors by using, in each model, the data

acquired during the scan of either internal hatches or borders. Fig. 12 shows that the use of the LHZ area alone yields a poor classification result, which is significantly improved by including the spatter descriptors into the model. In Build 1, slightly better classification performances were achieved by using the complete model (i.e., the one that includes both the LHZ area and the spatter descriptors), whereas in Build 2 this complete model and the one based on the spatter descriptors alone yield basically equal performances. Especially in Build 2, it is evident that exploiting only the data acquired during the scan of internal hatches enhances the classification performances. This is caused by the fact that the volumetric fluency levels were varied only during the internal scan phase. However, due to the interaction between the scan phase and the energy density highlighted in the previous sub-section, also the data acquired along the border scan entails relevant information for melting state classification.

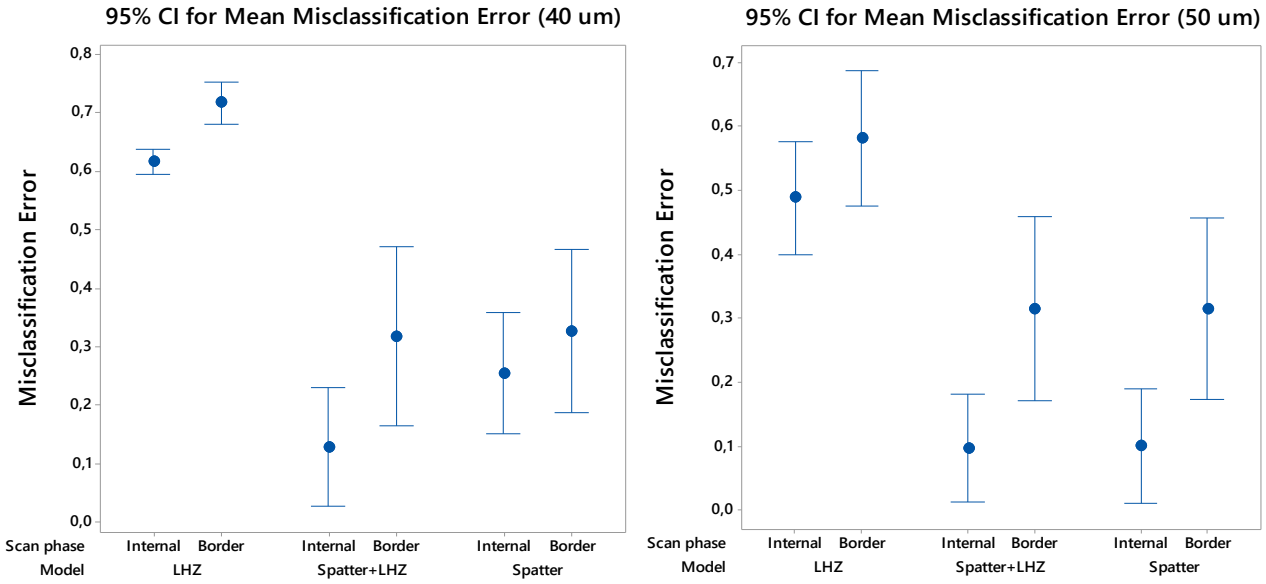

Fig. 12 – 95% CIs for the misclassification error estimated via leave-one-out cross-validation for different models in Build 1 (left panel) and Build 2 (right panel)

5. CONCLUSION

The development of in-situ sensing and process monitoring techniques represents a necessary step to overcome current technological barriers to the industrial breakthrough of metal AM systems. One major challenge consists of quickly detecting the onset of defects while the part is being produced. In this framework, our study focused on the monitoring of the process at track level. The objective was to evaluate the suitability of material ejections produced by the beam-material interaction is LPBF as potential observable signatures. Such additional type of information could be combined with other relevant quantities (e.g., the melt pool properties) to develop multi-sensor data fusion techniques to enhance the defect detection in LPBF.

The use of high-speed machine vision was discussed to gather in-situ image streams along the scan path of the laser and extract different statistical descriptors of the spattering behaviour. The selected descriptors captured the number, average size and spatial spread of the spatters during the scan of both internal hatches and borders. An experimental study involving specimens produced at different energy density levels (named under-, normal and over-melting) was carried out in LPBF of maraging steel powder. The results showed that the under-melting state yields a number of spatters with a spatial spread similar to the normal melting state, but with a smaller average area. Moreover, the over-melting state yields a larger number of spatters than the normal melting state with a larger spatial spread, but with a smaller average area. An ordinal logistic regression model was developed to evaluate whether spatter-related information could enhance the classification of out-of-control melting states with respect to the analysis of the laser heated zone alone. The comparative analysis confirmed that the in-situ analysis of spatters improves the capability of classifying different melting conditions. This suggests that spatters can be used as additional process signatures in LPBF process monitoring, possibly by coupling co-axial sensing for melt-pool monitoring with off-axial sensing for measuring additional quantities. Future research efforts will be aimed at including this kind of signature in statistical process monitoring tools based on in-situ image acquisition, possibly by comparing different sensing solutions. Further analysis are needed to investigate in more depth the spatial location effect on spatter descriptors where larger and more complicated slice geometries are produced, and to determine the suitability of spatter descriptors to detect transitory events and spatially localized defects.

REFERENCES

[1] Mani, M., Lane, B., Donmez, A., Feng, S., Moylan, S., & Fesperman, R. (2015). Measurement science needs for real-time control of additive manufacturing powder bed fusion processes. *National Institute of Standards and Technology, Gaithersburg, MD, NIST Interagency/Internal Report (NISTIR)*, *8036*.

[2] Tapia, G., & Elwany, A. (2014). A review on process monitoring and control in metal-based additive manufacturing. *Journal of Manufacturing Science and Engineering*, *136*(6), 060801.

[3] Everton, S. K., Hirsch, M., Stravroulakis, P., Leach, R. K., & Clare, A. T. (2016). Review of in-situ process monitoring and in-situ metrology for metal additive manufacturing. *Materials & Design*, *95*, 431-445.

[4] Spears, T. G., & Gold, S. A. (2016). In-process sensing in selective laser melting (LPBF) additive manufacturing. *Integrating Materials and Manufacturing Innovation*, *5*(1), 1.

[5] Sharratt, B. M. (2015). Non-Destructive Techniques and Technologies for Qualification of Additive Manufactured Parts and Processes. A literature Review. *Contract Report DRDC-RDDC-2015-C035*, *Victoria, BC*.

[6] Sames, W. J., List, F. A., Pannala, S., Dehoff, R. R., & Babu, S. S. (2016). The metallurgy and processing science of metal additive manufacturing. *International Materials Reviews*, 1-46.

[7] Craeghs, T., Bechmann, F., Berumen, S., & Kruth, J. P. (2010). Feedback control of Layerwise Laser Melting using optical sensors. *Physics Procedia*, *5*, 505-514.

[8] Craeghs, T., Clijsters, S., Yasa, E., Bechmann, F., Berumen, S., & Kruth, J. P. (2011). Determination of geometrical factors in Layerwise Laser Melting using optical process monitoring. *Optics and Lasers in Engineering*, *49*(12), 1440-1446.

[9] Craeghs, T., Clijsters, S., Kruth, J. P., Bechmann, F., & Ebert, M. C. (2012). Detection of process failures in layerwise laser melting with optical process monitoring. *Physics Procedia*, *39*, 753-759.

[10] Clijsters, S., Craeghs, T., Buls, S., Kempen, K., & Kruth, J. P. (2014). In situ quality control of the selective laser melting process using a high-speed, real-time melt pool monitoring system. *The International Journal of Advanced Manufacturing Technology*, *75*(5-8), 1089-1101.

[11] Berumen, S., Bechmann, F., Lindner, S., Kruth, J. P., & Craeghs, T. (2010). Quality control of laser-and powder bed-based Additive Manufacturing (AM) technologies. *Physics procedia*, *5*, 617-622.

[12] Lott, P., Schleifenbaum, H., Meiners, W., Wissenbach, K., Hinke, C., & Bültmann, J. (2011). Design of an optical system for the in situ process monitoring of selective laser melting (LPBF). *Physics Procedia*, *12*, 683-690.

[13] Kruth, J. P., Mercelis, P., Van Vaerenbergh, J., & Craeghs, T. (2007). Feedback control of selective laser melting. In *Proceedings of the 3rd international conference on advanced research in virtual and rapid prototyping* (pp. 521-527).

[14] Van Gestel, C. (2015). Study of physical phenomena of selective laser melting towards increased productivity. PhD Dissertation, Ecole Polytechnique Federale De Lausanne

[15] Yadroitsev, I., Krakhmalev, P., & Yadroitsava, I. (2014). Selective laser melting of Ti6Al4V alloy for biomedical applications: Temperature monitoring and microstructural evolution. *Journal of Alloys and Compounds*, *583*, 404-409.

[16] Doubenskaia, M., Pavlov, M., Grigoriev, S., Tikhonova, E., & Smurov, I. (2012). Comprehensive optical monitoring of selective laser melting. *Journal of Laser Micro Nanoengineering*, *7*(3), 236-243.

[17] Doubenskaia, M. A., Zhirnov, I. V., Teleshevskiy, V. I., Bertrand, P., & Smurov, I. Y. (2015). Determination of true temperature in selective laser melting of metal powder using infrared camera. In *Materials Science Forum* (Vol. 834, pp. 93-102). Trans Tech Publications.

[18] Chivel, Y. (2013). Optical in-process temperature monitoring of selective laser melting. *Physics Procedia*, *41*, 904-910.

[19] Pavlov, M., Doubenskaia, M., & Smurov, I. (2010). Pyrometric analysis of thermal processes in LPBF technology. *Physics Procedia*, *5*, 523-531.

[20] Kanko, J. A., Sibley, A. P., & Fraser, J. M. (2016). In situ morphology-based defect detection of selective laser melting through inline coherent imaging. *Journal of Materials Processing Technology*, *231*, 488-500.

[21] Krauss, H., Eschey, C., & Zaeh, M. (2012). Thermography for monitoring the selective laser melting process. In *Proceedings of the Solid Freeform Fabrication Symposium*.

[22] Krauss, H., Zeugner, T., & Zaeh, M. F. (2014). Layerwise monitoring of the selective laser melting process by thermography. *Physics Procedia*, *56*, 64-71.

[23] Lane, B., Moylan, S., Whitenton, E. P., & Ma, L. (2015). Thermographic Measurements of the Commercial Laser Powder Bed Fusion Process at NIST. In *Proc. Solid Free. Fabr. Symp* (Vol. 575).

[24] Bayle, F., & Doubenskaia, M. (2008, January). Selective laser melting process monitoring with high speed infra-red camera and pyrometer. In *Fundamentals of Laser Assisted Micro-and Nanotechnologies* (pp. 698505-698505). International Society for Optics and Photonics.

[25] Schilp, J., Seidel, C., Krauss, H., & Weirather, J. (2014). Investigations on temperature fields during laser beam melting by means of process monitoring and multiscale process modelling. *Advances in Mechanical Engineering*, *6*, 217584.

[26] Grasso, M., Laguzza, V., Semeraro, Q., & Colosimo, B. M. (2017). In-Process Monitoring of Selective Laser Melting: Spatial Detection of Defects Via Image Data Analysis. Journal of Manufacturing Science and Engineering, 139(5), 051001-1 - 051001-16.

[27] Jacobsmühlen, J., Kleszczynski, S., Schneider, D., & Witt, G. (2013). High resolution imaging for inspection of laser beam melting systems. In *2013 IEEE International Instrumentation and Measurement Technology Conference (I2MTC)* (pp. 707-712). IEEE.

[28] Jacobsmühlen, J., Kleszczynski, S., Witt, G., & Merhof, D. (2013). Elevated Region Area Measurement for Quantitative Analysis Of Laser Beam Melting Process Stability. In *Instrum. Meas. Technol. Conf. I2MTC* (pp. 707-712).

[29] Kleszczynski, S., Zur Jacobsmühlen, J., Sehrt, J. T., & Witt, G. (2012). Error detection in laser beam melting systems by high resolution imaging. In *Proceedings of the Solid Freeform Fabrication Symposium*.

[30] Zhang, B., Ziegert, J., Farahi, F., & Davies, A. (2016). In situ surface topography of laser powder bed fusion using fringe projection. *Additive Manufacturing*, *12*, 100-107.

[31] Foster, B. K., Reutzel, E. W., Nassar, A. R., Hall, B. T., Brown, S. W., & Dickman, C. J. (2015) Optical, layerwise monitoring of powder bed fusion. In *Solid Free. Fabr. Symp. Proc*, 295-307.

[32] Neef, A., Seyda, V., Herzog, D., Emmelmann, C., Schönleber, M., & Kogel-Hollacher, M. (2014). Low coherence interferometry in selective laser melting. *Physics Procedia*, *56*, 82-89.

[33] Land, W. S., Zhang, B., Ziegert, J., & Davies, A. (2015). In-situ metrology system for laser powder bed fusion additive process. *Procedia Manufacturing*, *1*, 393-403.

[34] Islam, M., Purtonen, T., Piili, H., Salminen, A., & Nyrhilä, O. (2013). Temperature profile and imaging analysis of laser additive manufacturing of stainless steel. *Physics Procedia*, *41*, 835-842.

[35] Dunbar, A. J. (2016). *Analysis of the Laser Powder Bed Fusion Additive Manufacturing Process Through Experimental Measurement and Finite Element Modeling* (Doctoral dissertation, The Pennsylvania State University).

[36] Thijs, L., Verhaeghe, F., Craeghs, T., Van Humbeeck, J., & Kruth, J. P. (2010). A study of the microstructural evolution during selective laser melting of Ti–6Al–4V. *Acta Materialia*, *58*(9), 3303-3312.

[37] Li, R., Liu, J., Shi, Y., Wang, L., & Jiang, W. (2012). Balling behavior of stainless steel and nickel powder during selective laser melting process. *The International Journal of Advanced Manufacturing Technology*, *59*(9-12), 1025-1035.

[38] Liu, Y., Yang, Y., Mai, S., Wang, D., & Song, C. (2015). Investigation into spatter behavior during selective laser melting of AISI 316L stainless steel powder. *Materials & Design*, *87*, 797-806.

[39] Khairallah, S. A., Anderson, A. T., Rubenchik, A., & King, W. E. (2016). Laser powder-bed fusion additive manufacturing: Physics of complex melt flow and formation mechanisms of pores, spatter, and denudation zones. *Acta Materialia*, *108*, 36-45.

[40] Gong, H., (2013) Generation and detection of defects in metallic parts fabricated by selective laser melting and electron beam melting and their effects on mechanical properties. *UofL Electronic Theses and Dissertations. Paper 515*.http://dx.doi.org/10.18297/etd/515

[41] Gao, X. D., Qian, W. E. N., & Katayama, S. (2013). Analysis of high-power disk laser welding stability based on classification of plume and spatter characteristics. Transactions of Nonferrous Metals Society of China, 23(12), 3748-3757.

[42] Zhang, M. J., Chen, G. Y., Zhou, Y., Li, S. C., & Deng, H. (2013). Observation of spatter formation mechanisms in high-power fiber laser welding of thick plate. Applied Surface Science, 280, 868-875.

[43] Nakamura, H., Kawahito, Y., Nishimoto, K., & Katayama, S. (2015). Elucidation of melt flows and spatter formation mechanisms during high power laser welding of pure titanium. Journal of Laser Applications, 27(3), 032012.

[44] You, D., Gao, X., & Katayama, S. (2014). Visual-based spatter detection during high-power disk laser welding. Optics and Lasers in Engineering, 54, 1-7.

[45] Grasso, M., Colosimo, B.M. (2017), Process Defects and In-situ Monitoring Methods in Metal Powder Bed Fusion: a Review, Measurement Science and Technology, 28(4), 044005.

[46] Kleinbaum, D. G., & Klein, M. (2010). Ordinal logistic regression. In Logistic Regression (pp. 463-488). Springer New York.

[47] Montgomery, D. C. (2008). Design and analysis of experiments. John Wiley & Sons.

[48] Sezgin, M., Sankur, B (2004), Survey over image thresholding techniques and quantitative performance evaluation. Journal of Electronic imaging, 13:146, pages.

[49] Chaki, N., Hossain Shaikh, S., Saeed, K. (2014), Exploring Image Binarization Techniques, Vol. 560 of the series Studies in Computational Intelligence, 5-15

[50] Hastie, T., Tibshirani, R., & Friedman, J. (2009). The elements of statistical learning, Springer New York.

APPENDIX A – The ordinal logistic regression model

Consider a classification problem characterized by a response variable, Y, with C ordered categories, and k explanatory variables $X_1, \dots, X_k$ for observations $i = 1, \dots, n$. The ordinal logistic regression model describes the relationship between the cumulative probabilities of the response categories and the explanatory variables. The probabilities associated to different categories are defined as $\pi^{(j)} = P(Y = j)$ and the probability that a response belongs to a category with a value less than or equal to category j is defined as $\gamma_i^{(j)} = P(Y_i \leq j)$ for the i-th observation. Then, the ordinal logistic regression model is defined as follows:

$$\ln\left(\frac{\gamma_i^{(j)}}{1-\gamma_i^{(j)}}\right) = \ln\left(\frac{P(Y_i \leq j)}{P(Y_i > j)}\right) = \alpha^{(j)} - (\beta_1 X_{1i} + \cdots + \beta_k X_{ki}), \qquad j = 1, \dots, C-1$$

Therefore, the model for the cumulative probabilities is:

$$\gamma^{(j)} = P(Y \leq j) = \frac{exp\left[\alpha^{(j)} - ((\beta_1 X_1 + \cdots + \beta_k X_k)\right]}{1 + exp[\alpha^{(j)} - ((\beta_1 X_1 + \cdots + \beta_k X_k)]}$$

The probabilities of individual categories are then computed as follows:

$$\pi^{(1)} = \gamma^{(1)} = \frac{exp\left[\alpha^{(1)} - ((\beta_1 X_1 + \cdots + \beta_k X_k)\right]}{1 + exp[\alpha^{(1)} - ((\beta_1 X_1 + \cdots + \beta_k X_k)]}$$

$$\pi^{(j)} = \gamma^{(j)} - \gamma^{(j-1)}$$

$$= \frac{exp\left[\alpha^{(j)} - ((\beta_1 X_1 + \cdots + \beta_k X_k)\right]}{1 + exp[\alpha^{(j)} - ((\beta_1 X_1 + \cdots + \beta_k X_k)]} - \frac{exp\left[\alpha^{(j-1)} - ((\beta_1 X_1 + \cdots + \beta_k X_k)\right]}{1 + exp[\alpha^{(j-1)} - ((\beta_1 X_1 + \cdots + \beta_k X_k)]},$$

...

$$\pi^{(C)} = 1 - \gamma^{(C-1)} = \frac{exp\left[\alpha^{(C-1)} - ((\beta_1 X_1 + \cdots + \beta_k X_k)\right]}{1 + exp[\alpha^{(C-1)} - ((\beta_1 X_1 + \cdots + \beta_k X_k)]}$$

Once the logistic regression model has been estimated, the classification task is accomplished by predicting the category probabilities for every observation and select the category with the highest probability.

Appendix B – Maraging powder specifications

The experimental analysis was performed by using a gas-atomized 18Ni (300) maraging alloy powder supplied by Sandvik Osprey LTD (Neath, UK). The particle size distribution is shown in Fig. B1 (the average particle size is about 35 µm). The alloy chemical composition in shown in Table B1 and Fig. B2 shows the morphology of a batch of powder used in the LPBF process.

Table B1 – Chemical composition of the maraging alloy (weight fraction, %)

Ni	Mo	Co	Ti	Al	Si
17.6	5.3	9.6	0.7	0.09	0.2

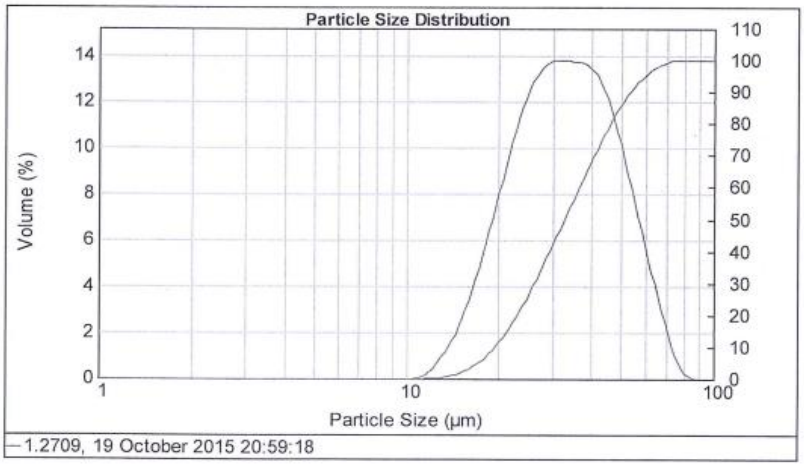

Fig. B1 – Particle size distribution of the maraging alloy powder used in the experimental activity

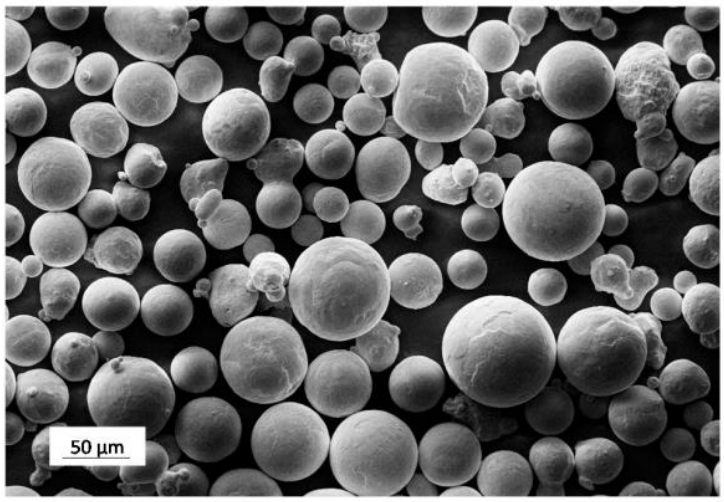

Fig. B2 – View of a batch of maraging alloy powder used in the experimental activity